Biomolecule Trafficking and Network Tomography-based Simulations

Charles Kervrann

Biomolecule Trafficking and Network Tomography-based Simulations

Charles Kervrann

Biomolecule Trafficking and Network Tomography-based Simulations

Charles Kervrann[a,1]

[a]*EPC Serpico, Inria Rennes, CNRS-UMR144, Institut Curie, PSL Research, Campus universitaire de Beaulieu, 35 042 Rennes Cedex, France*

ABSTRACT

During the past two decades many ground-breaking technologies, including Green Fluorescent Protein (GFP)-tagging and super-resolution microscopy, emerged and allowed the visualization of protein dynamics and molecular interactions at different levels of spatial and temporal resolution. In the meantime, the automated quantification of microscopy images depicting moving biomolecules has become of major importance in cell biology since it offers a better understanding of fundamental mechanisms including membrane transport, cell signaling, cell division and motility. Consequently, dedicated image analysis methods have been developed to process challenging temporal series of 2D-3D images and to estimate individual trajectories of biomolecules. Nevertheless, the current tracking methods cannot provide global information about biomolecule trafficking. This motivated the development of simulation techniques able to generate realistic fluorescence microscopy image sequences depicting trafficking of small moving particles in interaction, with variable velocities within the cell. In this chapter, we describe a simulation approach based on the concept of Network Tomography (NT) which is generally used in network communications and transport to infer the main routes of communication between origins and destinations. The trafficking model, scaled down for microscopy, is combined with real 2D-3D image sequences to generate artificial videos depicting fluorescently tagged moving proteins within cells. Simulation in bioimaging is timely since it has become essential to build ground truth datasets for image processing algorithm evaluation such as biomolecule detectors and trackers, as well as to generate training datasets for deep learning algorithms.

KEYWORDS

Fluorescence Microscopy, Intracellular Dynamics and Molecular Motion, Graphical Models, Network Tomography, Simulation and Image Synthesis

1. Email: charles.kervrann@inria.fr

1.1 MOTIVATION

The discovery of fluorescent labeling probes (Green Fluorescence Protein, Nobel Prize in chemistry 2008) and recent advances in optics and digital sensors (e.g. PALM (Photo Activated Localization Microscopy), STED (Stimulated Emission Depletion Microscopy) and SIM (Structure Illumination Microscopy)) have been key developments which have served to overcome the theoretical optical diffraction limit (200 nm) established in the 19th century. Because of these technological breakthroughs and their impacts in life sciences, contemporary microscopy has been praised through prestigious awards, such as the Nobel Prizes awarded to inventors of the concepts of super-resolution microscopy (2014) and cryo-electron microscopy (2017). Fluorescent microscopy imaging has become the spearhead of modern biology as it is able to generate videos comprising dozens of Gigabytes of data within an hour, and can depict long-term 4D nanoscale cell behaviors with low photo-toxicity. The ability to follow nanoscale cellular events is also proving to be of immense clinical relevance, especially for the study of cancer progression and viral infections. All these technological advances in microscopy have created new challenges for researchers in signal-image processing, and have even modified conventional paradigms once digital processing became a key component in the surmounting of the diffraction barrier (e.g. PALM, SIM).

In fluorescence microscopy systems record signals emitted by molecules tagged with genetically engineered proteins within cells. In a conventional setup photons are collected and registered at a given pixel (or voxel in 3D imaging). The measured fluorescence intensity is a scalar value, generally proportional to the density of tagged-molecules representing a few dozens of nanometers within a pixel/voxel (see Fig. 1.1). Fluorescence includes intensity (biomolecule density), wavelength (absorption and emission spectrum), time (fluorescence decay lifetime) and polarization (which arises from the dipole orientation). As the image data are 3D+Time signals, which could potentially depict several fluorescently tagged molecular species (multi-channel images), the interpretation of these signals represents a challenge in signal-image processing, and one for which several scientific barriers must be overcome. These barriers translate into un-solved challenges in image analysis, modeling, and simulation which need to be surmounted in order for this technology to be adopted in large-scale biological studies.

1.1.1 Traffic flows of biomolecules

Eukaryotic cells are characterized by membrane bound organelles. Their abilities to divide and fulfill their various functions within integrated tissues rely on the tight regulation of membrane composition, on the generation of ubiquitous and specialized organelles and on their capability to communicate with each other. Current research efforts in cell biology have already contributed to iden-

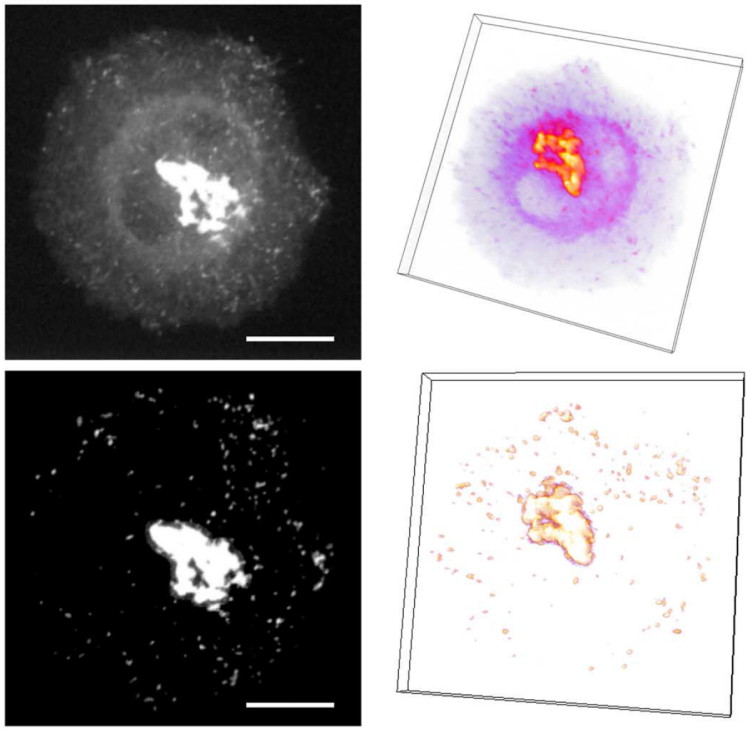

FIGURE 1.1 Acquisition of temporal series of 3D stacks in fluorescence spinning-disk confocal microscopy. (Left) One 2D image (top) extracted from a 3D stack depicting biomolecules (GFP-Rab6 proteins, see Section 1.3) in a single micro-patterned (disk-shaped) cell, and 2D image corresponding to the maximum projection of the 3D stack along the depth axis (bottom). (Right) Volume rendering of the fluorescent stack (top) and segmentation of transport vesicles and Golgi (bottom). The scale bars correspond to 5 μm.

tify hundreds of components defining key machineries of essential functions. It is well known now that, to preserve the structure, cohesion and functions of the organism, the eukaryotic cell exchanges biomolecules between its compartments and organelles: endosomes, Golgi apparatus, endoplasmic reticulum (ER)..., these intracellular exchanges require physical supports such as intermediate and actin filaments, and microtubules. Microtubules are polymers of tubulin that play an important role in a number of vital cell processes such as cell division, intracellular transport, and cell architecture. Furthermore, the transport pathways of biomolecules, mediated by vesicles propelled by molecular motors of the dynein and kinesin families along the cytoskeleton, provide the routes of communication between the organelles and the extra-cellular medium. The molecular motors transform chemical energy with the mediation of Adenosine

Tri-Phosphate (ATP) to mechanical work and driving energy for propelling the vesicles. It has also been established that transport from one compartment to the next one follows similar mechanistic principles, that is formation of coated vesicles, which bud from a donor compartment and then fuse with the recipient compartment. They involve similar protein networks controlling soluble and membrane protein sorting and vesicle formation, transport vesicle movement along cytoskeleton elements (actin nucleation machineries and molecular motors) and membrane fusion.

Nevertheless, it is still difficult to understand how these different machineries using multiple protein-protein and protein-lipid interactions are interconnected and coordinated in time and space during a given reaction like for intracellular transport, for instance. A long-term goal in fundamental biology is to decipher the dynamic coordination and organization of interacting molecules within molecular complexes at the single cell level and to explore the role of transport intermediates (e.g., vesicles) to higher levels of complexity, as during remodeling of the plasma membrane, differentiation and cell migration in contexts in forced two dimensions (micro-patterns), or in reconstituted three-dimensional environments. In that context, the mathematical and biophysical models, as well as estimation and simulation methods and algorithms, are particularly helpful to decode the traffic flows of biomolecules. Here, we focus on traffic simulation to describe the interactions between different cell compartments, membrane domains and organelles.

1.1.2 Biomolecule tracking and dynamics estimation

In fluorescence microscopy a first important challenge is to track and analyze the motion of biomolecules, with high precision, in 3D movies. This task is challenging because of the complexity of the dynamic processes being observed, such as association, dissociation, and recomposition of proteins, all of which are driven by interactions between several molecular species and further complicated by the particular phenomena of spatial coalescence related to image resolution. To that end a number of stochastic models have been proposed to describe the individual and collective motion of biomolecules [1, 2], including the jerky motions corresponding to switches between free diffusion (or Brownian motion), subdiffusion, and motor-mediated motion [3, 4].

It turns out that most existing methods are tracking techniques [5] requiring optimization or simulation in order to manage several thousands of tracks. The most commonly-used tracking approach is the so-called “connexionist” (or "detect-before-track") approach [6, 7, 8] which consists in detecting particles independently in each frame in a first step [9, 10], and then linking the detected particles over time. The related *data association* task is a critical step in this approach, especially if the number of particles is very high and if the trajectories interact. Multiple hypotheses tracking methods have then become popular [11, 12], where a set of data association hypotheses are generated to

account for all possible associations of tracking (or a suitable subset of those), identifying the most likely hypothesis according to some criterion. The aim of most Bayesian approaches for multiple object tracking [13] is to take into account the fact that the trajectories can cross each other, particles can move in and out of the frame, in and out of the depth of field, merge either by fusion to form a single particle, split into two or more particles, temporarily disappear due to mis-detection and so on. A very popular method is the U-track method [14] which robustly tracks spots and estimates heterogeneous motion in high density scenes whilst also exploiting recursive tracking in forward and backward temporal directions. U-track enables the prediction and the recovery of abrupt transitions, from freely (or confined) diffusive to directed motion, as well as the handling of spot disappearance. Thereafter several probabilistic methods have been designed to cope with different types of sub-cellular motion [15, 16]. All these methods were carefully evaluated a few years ago on the particle tracking challenge dataset [5], including robustness to noise and particle densities. It results that all trackers were very competitive, each performing at their best once on a target scenario.

Then, the tracks are exploited to infer molecular dynamics or mobility in cells. For instance, the mean-square displacement (MSD) method, which is widely used in biophysics and cell imaging, allows one to interpret biomolecule tracks and discriminate free, confined diffusion and directed flow since they represent the primary modes of mobility of molecules in living cells (see [10, 4]).

1.1.3 Network tomography for biomolecule trafficking modeling

The aforementioned tracking methods assume that the motion of individual particle car be represented by some known mathematical models, including Brownian motion or Markov models. Nevertheless, there is few satisfying modeling approaches able to represent the collective motion of particles and global biomolecule trafficking. In the specific case of vesicle trafficking within cells, collective motion can be inferred from the transport pathways that link "origin" regions to "destination" regions. The modeling is inspired from the Network Tomography (NT) concept, introduced to estimate vehicle traffic flows [17, 18], and further re-popularized to determine origin-destination traffic flows in computer networks [19].

In this general modeling, we consider a network defined as a graph $G(E,V)$ which consists of $|V|$ (cardinal of V) vertices and $|E|$ (cardinal of E) edges, where E and V denote the set of edges and vertices, respectively. Each pair of neighbor vertices is connected by two edges in order to enable traffic in both directions. A “toy” graph involving only four vertices is shown in Fig. 1.2 (top) for illustration. The particles are assumed to move from one vertex to another vertex by crossing edges. They follow a path defined by an origin vertex (or node), a destination vertex, and possible intermediate(s) vertex(ices). The set of paths can be then characterized by the origin and destination vertices, that is the

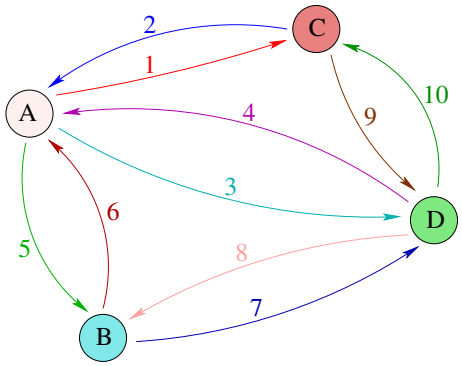

OD pair	*edge number*									
	1	*2*	*3*	*4*	*5*	*6*	*7*	*8*	*9*	*10*
$B \rightarrow A$	**0**	**0**	**0**	**0**	**0**	**1**	**0**	**0**	**0**	**0**
$B \rightarrow C$	**1**	**0**	**0**	**0**	**0**	**1**	**0**	**0**	**0**	**0**
$B \rightarrow D$	**0**	**0**	**0**	**0**	**0**	**0**	**1**	**0**	**0**	**0**
$\vdots$					$\vdots$					

FIGURE 1.2 4-nodes graph and routing matrix for Network Tomography. (Top) The vertices of the graph are labelled by letters and the edges by numbers. (Bottom) Several rows of the routing matrix **A** corresponding to the "toy" graph. The routing for the OD pairs is defined as the shortest paths using the Euclidean distance between vertices.

Origin-Destination pairs (OD pairs). Given $|V|$ vertices in the graph, the number K of possible OD pairs is $K = |V|(|V| - 1)$.

In NT, given the temporal measurements corresponding to the number of particles detected as going from one vertex to a neighbor vertex in the graph, the goal is to estimate the proportions of particles for each OD pair. More formally, let $x_{k,t}$ be the number of particles belonging to the path k that joins the "Origin" node to the "Destination" node (OD pair k) at time t. The measurements $z_{e,t}$ correspond to the number of particles that pass through edge e at time t. In the traffic flow problem, we then assume the following model:

$$\boldsymbol{Z} = \mathbf{A}\boldsymbol{X}, \tag{1.1}$$

where $\boldsymbol{Z} = \{z_{e,t}\}_{e\in\{1,\cdots,|E|\},\, t\in\{1,\cdots,T\}}$ and $\boldsymbol{X} = \{x_{k,t}\}_{k\in\{1,\cdots,K\},\, t\in\{1,\cdots,T\}}$ are matrices and denote the set of measurements and the unknown OD flows, respectively, and T is the number of images in the sequence. Here, $\mathbf{A}$ denotes the $|E| \times K$ routing matrix with binary elements: $a_{e,k} = 1$ if edge e belongs to the path for the OD pair k, and 0 otherwise. Usually, it is assumed that there exists a single path for one OD pair defined as the shortest path in the graph. Further-

more, a cost is associated to each edge and the Dijkstra algorithm [20] is applied to the whole graph for computing the shortest path for each OD pair. In Fig. 1.2 (bottom), we show a few rows of the binary routing matrix $\mathbf{A}$ corresponding to the graph shown in Fig. 1.2 (top) when the Euclidean distance between the vertices is considered.

In NT, the traffic flow problem (1.1) aims at estimating the matrix $\boldsymbol{X}$ given the routing matrix $\mathbf{A}$ and the counting measurements $\boldsymbol{Z}$. This problem is an *under-constrained* problem since K is greater than $|E|$ (see (1.1)). If we are only interested in the proportions of particles on each OD pair, we need to solve the following optimization problem:

$$\min_{\bar{\boldsymbol{x}}} \|\bar{\boldsymbol{z}} - \mathbf{A}\bar{\boldsymbol{x}}\|^2 \text{ subject to } \bar{x}_k \geq 0,\ k \in \{1, \ldots, K\}, \tag{1.2}$$

where $\bar{\boldsymbol{x}} = (\bar{x}_1, \ldots, \bar{x}_K)^T$ contains the positive proportions of particles for each OD pair and $\bar{\boldsymbol{z}} = (\bar{z}_1, \cdots, \bar{z}_{|E|})^T$ corresponds to temporal averages. Additional constraints can be considered. For instance, Vardi proposed a Poisson distribution for $\bar{\boldsymbol{x}}$ because the data are counts [19]; as there is a lot of possible OD pairs but at the same time the traffic is observed only on a few of them, one can prefer to impose a sparsity constraint as follows:

$$\min_{\bar{\boldsymbol{x}}} \|\bar{\boldsymbol{z}} - \mathbf{A}\bar{\boldsymbol{x}}\|^2 + \lambda\|\bar{\boldsymbol{x}}\|_0 \text{ subject to } \bar{x}_k \geq 0,\ k \in \{1, \ldots, K\}, \tag{1.3}$$

where $\lambda > 0$ is weighting parameter and $\|\bar{\boldsymbol{x}}\|_0 = \#\{\bar{x}_k \neq 0\}$, $k \in \{1, \ldots, K\}$.

1.2 SIMULATION FOR BIOMOLECULE TRAFFICKING ANALYSIS

In this section, we describe a Network Tomography-based simulation framework able to generate complex motions and interactions between moving particles with variable velocities within the cell. We design graphical representations and dynamical models built from representative fluorescence microscopy image sequences. These representations are exploited to generate artificial image sequences that mimic biomolecules trafficking observed in real image sequences.

1.2.1 History and state of the art

In biomedical imaging, simulations are required for validating physical models, understanding recorded data, evaluating the performance of image analysis algorithms [5], or training complex models from large-scale synthetic datasets as recently investigated with supervised Deep Learning methods [21, 22]. Nevertheless, the proposed simulation methods used to build benchmarking data sets are limited yet since they are not able to represent the whole complexity of interacting biomolecules as observed in real image sequences.

In past years, random walks combined with parametric drift models (e.g. [23]) and diffusion models in sub-regions in the cell [21] were considered for simulating images depicting biomolecule motions. A more realistic approach

consists in simulating particles undergoing stochastic motions depending on interactions with the cytoskeleton and the cytosol within the cell as described in [24]. The intracellular particles move along the microtubule network via molecular motors, or diffuse in the cytosol. Formally, a transport vesicle is generally represented by a particle $p(t) \in \mathbb{R}^d \times \{1, \cdots, T\}, d = 2,3$ whose dynamics follows a stochastic rule [24]:

$$dp(t) = \begin{cases} \sqrt{2K_d}\, dw(t) & \text{if } p(t) \text{ is free within the cytosol,} \\ V_m & \text{if } p(t) \text{ is bound to a microtubule,} \end{cases} \tag{1.4}$$

where w is Brownian motion, $K_d \in \mathbb{R}$ is the diffusion constant in the cytosol, and V_m is the constant drift motion along the microtubules. Thus, a given transport vesicle switches between diffusion in the cytosol (Brownian motion) and active motion along microtubule (directed motion). The molecular motor allows the vesicle to be propelled at a given speed V_m. In [24], the cells are assumed to be flat and the cytosol is represented by a two-dimensional ($d = 2$) ring of maximum radius (outer membrane of the cell) and minimum radius (nuclear envelope). The microtubules are uniformly and radially distributed, coming from the nucleus towards the outer membrane. In this line of modeling work, Klann et al. proposed an alternative mechanistic agent-based simulation able to combine signal transduction and membrane trafficking, to study the effect of receptor-mediated endocytosis on signaling [25].

More generally, two modeling approaches have been investigated for simulation at the scale of single cell in past years: *data-driven modeling* and *physics-based modeling*. The physics-based approach relies on the physical properties of the components in the cell. The main advantage is that the model parameters are easily interpreted as they are well grounded in biophysics. This approach is generally considered to investigate complex spatiotemporal biological events, for instance to study the dynamics of microtubule networks [26, 27, 28], or to characterize diffusion of biomolecules in nano-domains [21]. By tuning the control parameters, an expert can artificially generate dynamics which are visually similar to those observed in real data, provided that the underlying dynamical models are well designed. The data-driven modeling aims at describing image sequences through statistical models learned from real images. This approach can only "imitate" dynamical processes but is not able to fully transcribe the physical properties of dynamical processes. However, unlike physics-based modeling, the data-driven approach can capture the features of complex multi-scale systems as a whole. The data-driven and physics-based approaches can also be gently combined to model the main components of the image sequence, as recently investigated in [22] to mimic calcium dynamics in astrocytes observed in lattice light sheet microscopy.

Finally, by minimizing the discrepancy between a set of descriptors computed from a real image sequence and the same set of descriptors computed from a simulated sequence, the parameters of the simulation method can be tuned to obtain

an artificial sequence that reveals apparently the same dynamical characteristics as the observed sequence. This line of research is related to data assimilation, developed on a controlled trade-off between observations of a phenomena and a model accounting for its likely dynamics.

1.2.2 Network tomography-inspired simulation

The simulation approach falls in the category of data-driven methods and exploits real image sequences as inputs. In the simulation scenario, the fluorescence-tagged biomolecules are assumed to be transported via transport vesicles propelled by molecular motors along the cytoskeleton composed of actin filaments, intermediate filaments, as well as microtubules. Here, we focus on microtubules which are polymers with a diameter of about 25 nm. They have an exceptional bending stiffness and form a dense network (see illustration in Fig. 1.3(b)). The dynein and kinesin proteins are two classes of molecular motors associated with microtubules. In stable conditions, the speed and polarization of these motors is assumed to be constant. This explains partially why the observed velocity of vesicles is constant if they move along the same microtubule. In the simulation framework, we assume that the microtubule network is static when compared to moving biomolecules.

Modeling of transport vesicle appearance. In video-microscopy, the vesicles appear as small bright spots against a dark background (Figs. 1.3 (a) and 1.4). The vesicle diameter theoretically ranges from 60 to 150 nm, that is below the spatial resolution of the microscope which is about 200 nm. However, the point spread function of the microscope makes them appear as larger structures in acquired images. As illustrated in Fig. 1.4, the stretching is more significant as the vesicle moves rapidly. Furthermore, when the density of objects increases, the vesicles gather together and constitute small rods. Consequently, large vesicles or sets of nearby vesicles can be satisfyingly represented by anisotropic Gaussian spots as proposed in [30, 23] with variances related to the spot dimensions ranging from 60 to 150 nm, which is very close to the pixel size. In the simulation framework, the covariance matrix of the anisotropic Gaussian spot is a function of the displacement direction. The ellipticity also depends on the velocity, induced by molecular motors bound to the microtubules. Figure 1.5 schematically illustrates how the covariance matrix of the anisotropic Gaussian function allows one to modify the orientation of spots according to the direction of the microtubule axis. As we wish to simulate image sequences close to those acquired with a spinning disk microscope, we first measure the maximum intensity of a large number of vesicles on real sequences, which approximately follows a Gaussian distribution.

Modeling of microtubule network. In order to generate a synthetic but realistic microtubule network, we exploit real image sequences as input for the

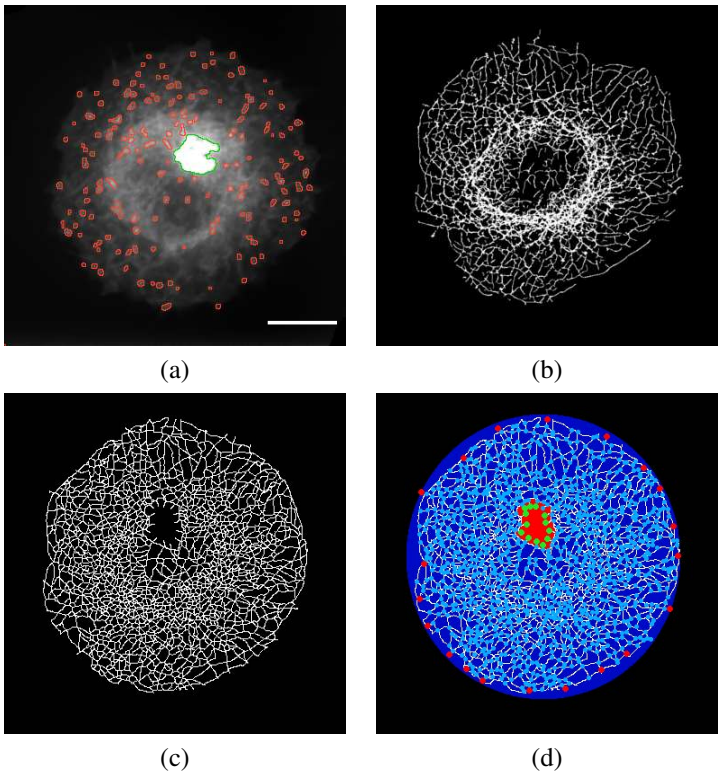

FIGURE 1.3 Biomolecule trafficking in cells. (a) GFP-Rab6 vesicles in micro-patterned (disk-shaped) cell where the Golgi and the vesicles are delineated with green and red curves, respectively. (b) Fluorescently tagged microtubule network. (c) Extraction of a microtubules network from (b) by applying a dedicated algorithm [29] and manual correction. (d) Labeling of nodes (blue) and edges (white) of the network. The origin and destination nodes are depicted in green and red, respectively. The scale bar corresponds to $5\mu m$.

modeling. A real network can be tagged with green fluorescence protein (GFP) as illustrated in Fig. 1.3(b) but this network is generally very complex and individual microtubules cannot be easily extracted (see Fig. 1.3(c)). Alternatively, the microtubule network can be coarsely obtained from the maximum intensity projection (MIP) map with respect to time, that is from the paths followed by the tagged vesicles. The bright paths in the MIP map enlighten the main routes used by the vesicles, assumed to be the traffic motorways of the microtubule network. Figure 1.6(a) shows the MIP image of a real 2D sequence of 300 images acquired with a spinning disk confocal microscope, defined as:

$$\mathrm{MIP}(I)(s) \quad = \quad \max_{t\in\{1,\cdots,T\}} I(s,t),\ \forall s \in \Omega, \tag{1.5}$$

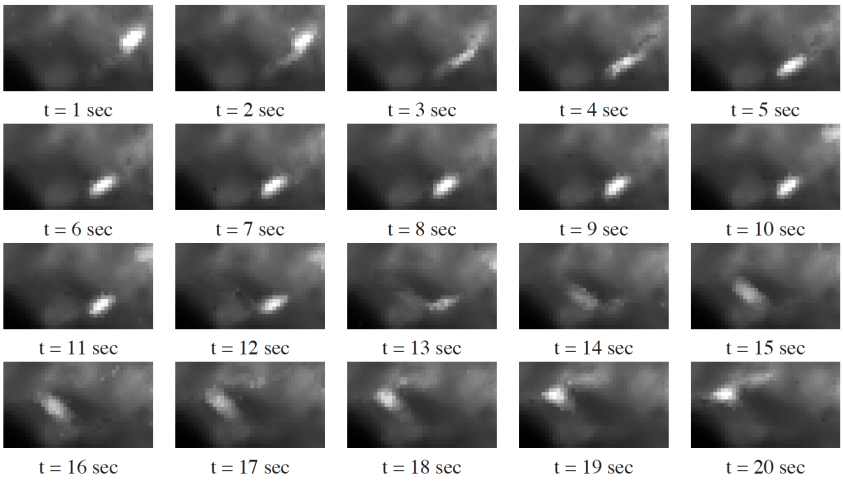

FIGURE 1.4 Appearance of vesicles in cells. Twenty regions of interest extracted from a real spinning disk confocal microscopy image sequence in which a vesicle (bright spots) moves from right to left.

where T denotes the number of images in the sequence, and $I(s,t)$ is the fluorescence intensity observed at time t and at pixel s in the image domain Ω. This simple projection allows one to select the main routes used for the intracellular trafficking, leading to a network with lower complexity. In practical imaging, the routes are extracted by applying an appropriate line detection algorithm [29] and by manually adding segments to complete the discontinued paths (see Fig. 1.6(b)). The fluorescent background is preliminary removed by applying dedicated algorithms (e.g. [31]). Each route is defined by a list of points, and each point of this list is parameterized by the width of the road, and its orientation. Finally, the crossing between routes serve to detect nodes which are further labelled as "origin" nodes and "destination" nodes, according to NT (see Fig. 1.6(b)).

Modeling of particle trafficking. According to the NT concept, the vesicles are transported along the microtubule network from origin nodes to destination nodes. The network microtubule is represented by a graph and trafficking is driven by the routing matrix. The first step of the modeling consists in building a graph from the microtubule network automatically extracted from real images as explained above. Each intersection and each end-point is labeled as a vertex of the graph G. The $|V|$ vertices form the set $V = \{v_1, \cdots, v_{|V|}\}$ and each connection between two vertices is associated with two edges allowing to establish the transport of particles in both directions. The $|E|$ edges constitute the set $E = \{e_1, \cdots, e_{|E|}\}$.

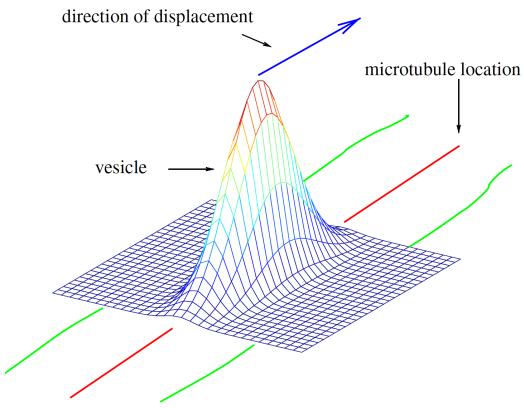

FIGURE 1.5 Gaussian model of the spot oriented in the direction of the microtubule axis. The covariance matrix of the Gaussian function depends on the velocity of the vesicle. The simulated vesicles are then elongated along with the displacement direction. The anisotropic Gaussian spots have an average length of 180 nm and a standard deviation of 90 nm.

In the next step, an Origin-Destination (OD) pair is characterized by an origin vertex and a destination vertex in the graph. The user specifies a certain number of OD pairs among the $K = |V|(|V| - 1)$ possible OD pairs, and assigns to each of them a proportion of traffic. The routing is used to complete the description and aims at establishing a list of successive edges in the graph to derive an OD pair, corresponding to one or more paths, to connect an origin node to a destination node. The basic approach consists in assigning one path to only one OD pair. The resulting routing matrix is generally a binary matrix, as considered in telecommunication networks (see Fig. 1.2). Nevertheless, as all vesicles do not necessarily take the same routes for a uniquer origin node to reach a destination node, we identify, instead, all possible paths in the graph for each OD pair. The shortest paths are especially used to transport the vesicles and are identified with appropriate algorithms such as the Yen's algorithm [32]. A cost $C(\Gamma)$ is assigned to each path Γ and defined as the sum of costs $\{c(e_j)\}$ attached to edges $\{e_1, \cdots, e_{|E|}\}$: $C(\Gamma) = \sum_{j=1}^{N(\Gamma)} c(e_j)$, where $N(\Gamma)$ denotes the number of edges in the path Γ. In what follows, the cost $C(\Gamma)$ is proportional to the path length and is translated into a probability as follows:

$$P(\Gamma) \propto \exp\left(-\frac{C(\Gamma)}{\kappa}\right), \tag{1.6}$$

where $\kappa > 0$ is a parameter used to encourage "short" paths (if κ is small); if κ is very large, the probabilities are the same for all paths. All the probabilities are then used to establish the routing matrix $\mathbf{A}$ of dimension $|E| \times K$ and to determine the prior distribution of paths. Let $\{\Gamma_{e,k}^{\ell}\}, \ell = \{1, \cdots, L\}$, be the set

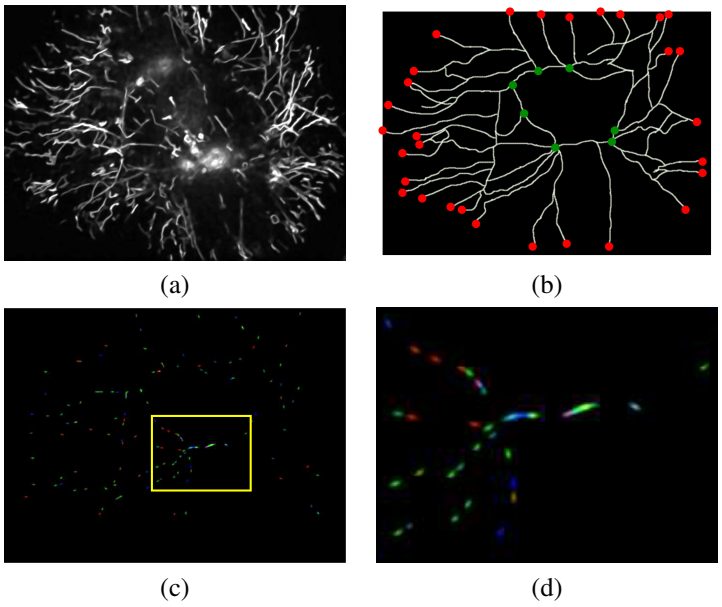

FIGURE 1.6 Design of traffic network for GFP-Rab6 proteins in a single cell. (a) Maximum intensity projection (MIP) map built from 300 images. (b) Extraction of microtubules network (white curves) and graph made of 159 nodes and 398 directed edges. The expert manually selected origin nodes (green balls) in the central part of the network (small ring) while the destination nodes (red balls) are located at the periphery. (c) Simulated image at time $t = 250$. Vesicles are only going from the Golgi (central region) to the "end-points" located at the periphery of the cell. Thus, the retrograde transport from "end-points" to Golgi is prohibited and assumed to be inhibited by bio-chemical alterations. Among the 25,122 possible origin-destination pairs, 252 origin-destination pairs were observed in this simulated image sequence. (d) Zoom-in view of the region of interest delineated by a yellow rectangle in (c).

of paths for a given OD pair k, that use the edge e, and $P(\Gamma_{e,k}^{\ell})$ denotes the associated probabilities. For a given OD pair k, we compute the elements of matrix $\mathbf{A} = \{a_{e,k}\}$ as follows:

$$a_{e,k} = \frac{\sum_{\ell=1}^{L} P(\Gamma_{e,k})}{\sum_{e'=1}^{|E|} \sum_{\ell=1}^{L} P(\Gamma_{e',k})}. \tag{1.7}$$

In summary, the strategy for simulation consists then in assigning a vesicle to an OD pair and drawing path depending on prior probabilities (1.6). The dynamics of particles is fully established from the routing matrix $\mathbf{A}$. Here, at each time step Δt, the vesicle is moved along the microtubule with a displacement step which is a proportional to the velocity. To display the vesicles in each image of the sequence as illustrated in Figs. 1.6(c)-(d), the appearance model presented earlier and illustrated in Fig. 1.5, is used.

Modeling of dynamical events.

Let p be a particle assigned to an OD pair and Γ_p be a path among the shortest paths that join the origin and destination nodes of the OD pair. Let γ_p be the curve in the image domain associated to the path Γ_p. At the initialization, the vesicle is positioned at the origin of the curve γ_p. Then, it moves with variable velocities depending on curvature until it reaches its destination node, and then disappears. Nevertheless, in real image sequences, we observed additional events corresponding to "stop-and-go" [33], which may be induced by traffic congestion. These events are taken into account in the simulation framework as follows.

Let $E(p,t) = \{S, M, PS\}$ be the state of the vesicle p at time t, where 'S', 'M' and 'PS' denote the "Stop", "Motion", and "Pseudo-Stable" states, respectively. A proportion of particles located in the neighborhood of the destination node, are in the "Pseudo-Stable" state just before reaching the destination node. Formally, it means that the vesicle p stops during a time interval T_{PS}. Hence, at the initialization, a binary variable $b_p \in \{0,1\}$ is drawn according to a Bernouilli distribution (with probability P_{PS}); if $b_p = 1$, the particle p will stop transiently before reaching the destination node. The position $r_p(t+\Delta t)$ of the particle p at time $t+\Delta t$ along the curve γ_p is then defined as follows:

$$r_p(t+\Delta t) = \begin{cases} r_p(t) + V_p(t)\Delta t & \text{if } E(p,t+\Delta t) = M \\ r_p(t) & \text{if } E(p,t+\Delta t) = S \\ r_p(t) & \text{if } E(p,t+\Delta t) = PS \end{cases} \tag{1.8}$$

where $V_p(t)$ denotes the velocity of the particle along the curve γ_p. Furthermore, we define the transition probabilities to switch from one state to another as follows:

- Probability to stop at time $t+\Delta t$ ($M \rightarrow S$):

$$P(E(p,t+\Delta t) = S \mid E(p,t) = M) = P_{M\rightarrow S}.$$

- Probability to re-start at time $t+\Delta t$ ($S \rightarrow M$):

$$P(E(p,t+\Delta t) = M \mid E(p,t) = S) = P_{S\rightarrow M}.$$

- Probability to stop transiently at time $t+\Delta t$ such as $0 \leq t \leq T_D$ ($M \rightarrow PS$):

$$P\left(E(p,t+\Delta t) = PS \mid E(p,t) = M,\ b_p = 1, |t - T_D| < \alpha T_D\right) = P_{M\rightarrow PS}$$

  where $0 \leq \alpha \leq 1$ and T_D is the time necessary to reach the destination node.
- Probability to re-start at time $t+\Delta t$ in the neighborhood of the destination node ($PS \rightarrow M$):

$$P(E(p,t+\Delta t) = M \mid E(p,t) = PS, E(p,t - T_{PS}(p))) = P_{PS\rightarrow M}.$$

The particle p is "Pseudo-Stable" during the time interval $T_{PS}(p)$, uniformly drawn in the interval $[T_{PS}^{min}, T_{PS}^{max}]$. The probability to switch to the Pseudo-Stable" state is determined by b_p and the spatial position of the particle $r_p(t)$ along the curve γ_p with respect to the position of the destination node.

Finally, we have consider additional events such as "fusion" events when two particles p_1 and p_2 are located on the same pixel in the image domain at time t. The "fusion" event is an unlikely event and the corresponding probability is denoted P_F. If the particles are fused, the new particle p is assigned to one of the two OD pairs with the same probability. Finally we consider "turnaround" events suggesting that the particle moves back and takes another path with probability $P_T = P(\Gamma_p \rightarrow \Gamma_p^{'})$ to reach the destination node.

As all these probabilities cannot be set *a priori*, they are determined from the analysis of particle trajectories estimated given real image sequences.

1.3 APPLICATIONS

In this section, we give a few examples of simulation, including experiments with real images depicting GFP-Rab6 vesicle trafficking. Rab6 is a member of the Rab family of small GTPases, which is involved in the vesicle budding, docking, tethering, and fusion steps during transport. It was well established that it regulates retrograde transport from the Golgi complex to the Endosplamic Reticulum [34]. In real experiments, we used HeLa cells stably transfected with GFP-tagged proteins. The HeLa cell line is a human cancer continuous cell line. The most attractive properties of HeLa cells is the ability to proliferate indefinitely and to multiply rapidly (< 24 hours). These properties make them the perfect cell line to study molecular mechanisms of carcinogenesis. Temporal series of $380 \times 380 \times 8$ stacks were acquired with a confocal microscope equipped with spinning disk system (voxel resolution: $64.5\ nm \times 64.5\ nm \times 300\ nm$; frame rate: one stack per second).

1.3.1 Simulation of toy examples

First, we consider a very simple network which is manually defined inside a square domain of 128×128 pixels. The network is composed of five nodes and sixteen edges corresponding to eight routes (see Fig. 1.7). We selected two origin nodes (1 and 3) and two destination nodes (2 and 4). We then generated the movements of 20 spots started from the two origin nodes. In Fig. 1.7, each moving spot is assigned a particular color. At the initialization ($t = 0$), all the vesicles are located inside the vicinity of two origin nodes. Therefore, the fluorescence concentration is relatively high. Later on, the collective movements of individual vesicles form trains after a few seconds. Because of the different paths taken by them and the variance of their velocities, the packets diffuse, and eventually the vesicles are distributed over the whole network.

In the second example, we apply the simulation framework to generate a

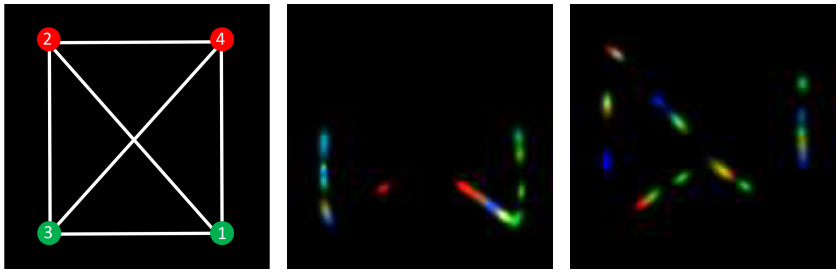

FIGURE 1.7 Simulation of a sequence from a 4-node network. (Left) Network composed of routes, two origin nodes (1 and 3) and two destination nodes (2, 4). (Right) Movements of 20 artificial vesicles at time $t = 0$ and $t = 500$, respectively. Each moving spot is assigned a particular color.

synthetic image sequence based on the network shown in Fig. 1.8 (b)(c). An image extracted from this sequence is shown in Fig. 1.8 (d). The simulated image sequence is composed of 121 images containing 1000 moving vesicles in the whole sequence. The vesicles are moving from the center region (green) in the network to "end-points" (red) located at the periphery of the image (see Fig. 1.8(c)). For each generated vesicle, a destination among all the possible "end-points" is selected to ensure that the distribution of vesicles is uniform on all OD pairs.

A last example is shown in Fig. 1.9 and depicts a hand-crafted network (a) composed of 25 nodes and 70 edges corresponding to 35 routes. The origin nodes (green) are the nodes located at the top right of the image while the destination nodes (red) are the nodes located at the bottom left. Twenty vesicles are superimposed on a dynamical background modeled as linear function of time, to mimic real fluorescence image sequences. The background intensity $I_B(s,t)$ at pixel $s \in \Omega$ and time t is represented as follows: $I_B(s,t) = a_0(s) + a_1(s)t$. The coefficients $a_0(s)$ and $a_1(s)$ varies with the spatial image position and are shown in (b) and (c), respectively. Two typical images extracted from a $128 \times 128 \times 150$ image sequence are shown in (d-e). The intensity of the 20 moving vesicles is assumed to follow a Gaussian law with mean 30 and standard deviation 3.

1.3.2 Simulation of GFP-Rab6 vesicle trafficking

In this section, we demonstrate the interest of the simulation methods to study the GFP-Rab6 vesicular trafficking in single micro-patterned cells. It has been established that Rab6 proteins are transiently anchored to moving transport carriers from the Golgi apparatus located at the cell center to Endoplasmic Reticulum entry sites or to plasma membrane [34, 35, 36, 37, 38, 39], both

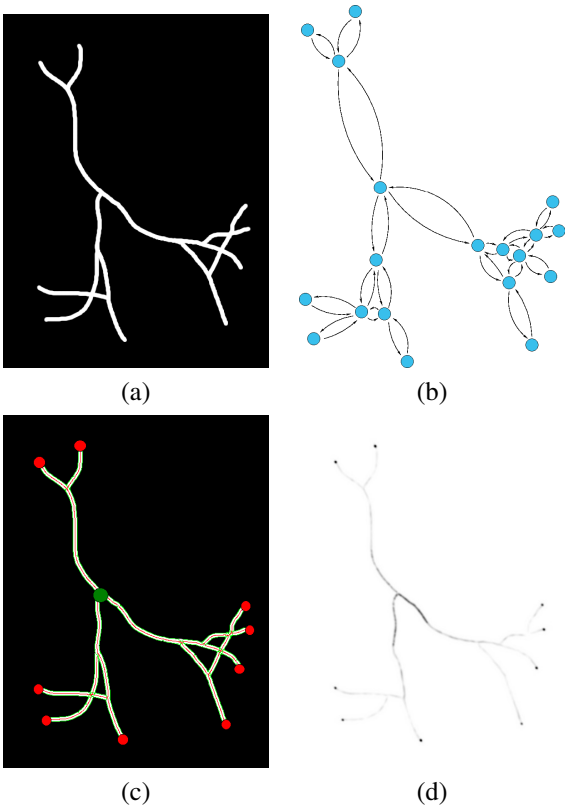

FIGURE 1.8 Simulation of a sequence from a simple microtubule network. (a) Simplistic microtubule network. (b) Associated graph. (c) Network for traffic. The origin vertex is labelled in green while the destination vertices are labelled in red. (d) One image extracted from the whole simulated image sequence.

assumed to be located at the cell periphery, where they should dissociate from membranes and recycle back to the cytosol.

In this study, shapes of the cells are constrained with micro-fabricated patterns [40] (see Figs. 1.10, 1.13 and 1.14). Micro-patterning is a well-established strategy to reduce morphological variability by imposing constraints on adhesion sites, which has been shown to influence the cytoskeleton geometry and transport vesicle localization [40, 41, 42] and cellular endomembranes at the steady state within fixed cells [43].

Preliminary experiments about GFP-Rab6 vesicle traffic orientation. In this preliminary experiment, we demonstrate the dynamical orientation of Rab6 positive membranes in disk-shaped cells. According to the expert-biologists, the

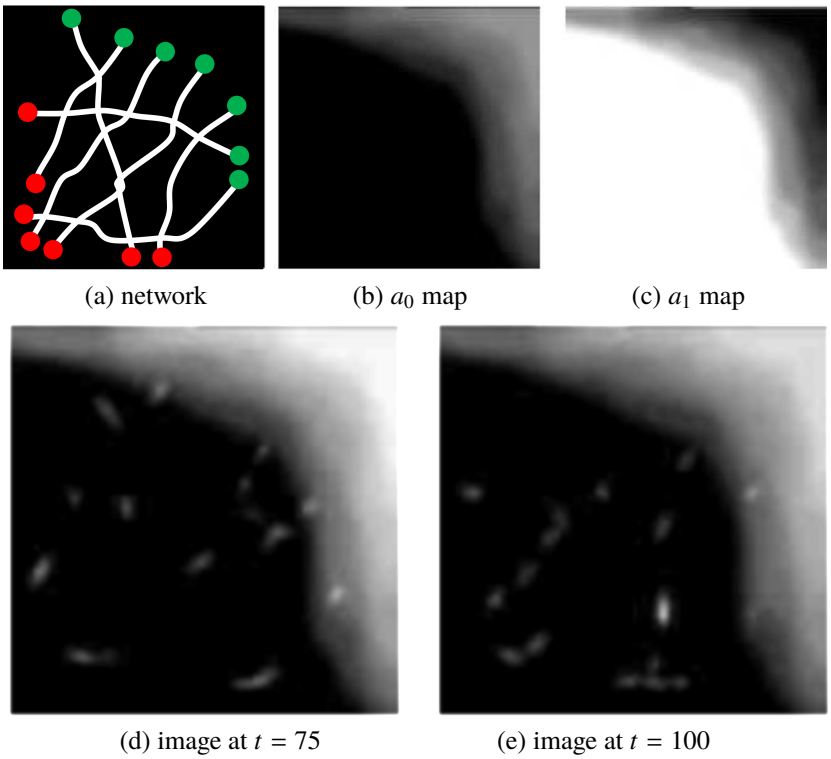

(a) network (b) a_0 map (c) a_1 map

(d) image at $t = 75$ (e) image at $t = 100$

FIGURE 1.9 Simulation of an image sequence with background. (Top) Network (a) composed of 7 origin (red balls) and 7 destination nodes (green balls), and background components a_0 and a_1 in (b) and (c), respectively. (d-f) Movement of 20 vesicles at time $t = 75$ and 100, respectively, with superimposed background I_B.

vesicles mostly move from the Golgi Apparatus to "end-points" located at the periphery of the cell. Accordingly, we analyzed the Rab6 vesicles fluxes with a suitable image partition composed a central region, a crown, and additional peripheral regions (see Fig. 1.11 (right)). The vesicles and Golgi are detected and segmented by applying dedicated algorithms (e.g. C-CRAFT [31], ATLAS [44] (see Fig. 1.10). The particle centers are defined as the mass centers of the connected components extracted from the segmentation mask. From these coordinates, the temporally-varying number of particles in every region of the image partition has been computed, while discarding the Golgi region (central region) as trafficking is not occurring in this particular region. By applying a dedicated algorithm [45], we estimated the vesicle fluxes are furthermore grouped according to four different categories related to direction (see Fig. 1.11): i) fluxes towards the cell periphery (green arrows in cell partitions); ii) fluxes towards the Golgi (red arrows); iii) lateral fluxes in the inner crown

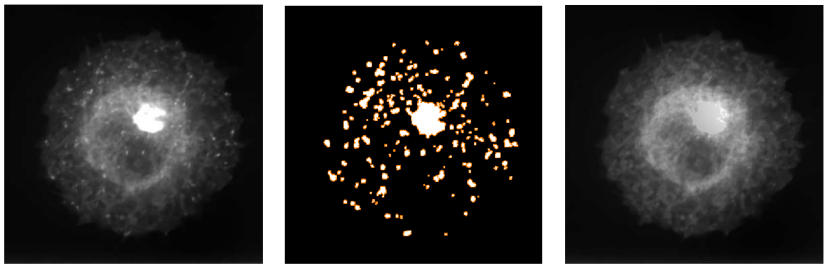

(a) (b) (c)

FIGURE 1.10 Background estimation and vesicle detection. Application of C-CRAFT algorithm [31] to a disk-shaped cell image sequence (a) for vesicle detection (b) background estimation (c).

(purple arrows); iv) lateral fluxes in the outer crown (blue arrows).

This study confirmed that the Rab6 positive membranes predominantly move to the cell periphery (as lateral directions are divided into two opposite directions, corresponding to $2 \times 20\%$). Here, we divided the lateral directions into two different categories to evaluate if the vesicles have the same behavior when they are close to the Golgi or close to the cell periphery. The results are reported in Fig. 1.11 (bottom). These results demonstrate that for micro-patterned cells, Rab6 positive membranes are predominantly trafficking towards the cell periphery. The lateral fluxes in the outer crown are more important than lateral fluxes in the inner crown. This indicates that GFP-Rab6 vesicles trafficking is more directed in regions close to the Golgi than in regions located at the cell periphery. This behavior is related to the vesicle docking step that is happening before vesicle reach their end-point.

Simulation of GFP-Rab6 dynamics. We applied the simulation framework described in Section 1.2.2 to mimic GFP-Rab6 vesicle dynamics as observed in spinning disk microscope images. A first simulated image sequence is shown in Fig. 1.12 (b)-(d). The traffic is here uniformly distributed over each OD pair. The microtubule network, estimated from temporal series of volumes ($64.5 \times 64.5 \times 300\ nm^3$) is composed of 157 vertices (Fig. 1.12 (a)), involving 24,492 OD pairs. Three typical images extracted are shown in Fig. 1.12 (b)-(d). In Table 1.1, we reported the typical values used to simulate this image sequence.

Meanwhile, we investigated two different cell geometries, the crossbow-shaped pattern and the circular-shaped pattern. The speed of the vesicles ranges from 1 to 10 pixels and the number of objects can be large (about a few hundreds). Several consecutive images (1 frame/sec) extracted from both the real and simulated sequences are shown in Figs. 1.13 and 1.14. To assess the quality of simulated images sequences, we compare the images at time t and intensity projections along the temporal, including the Maximum Intensity Projection

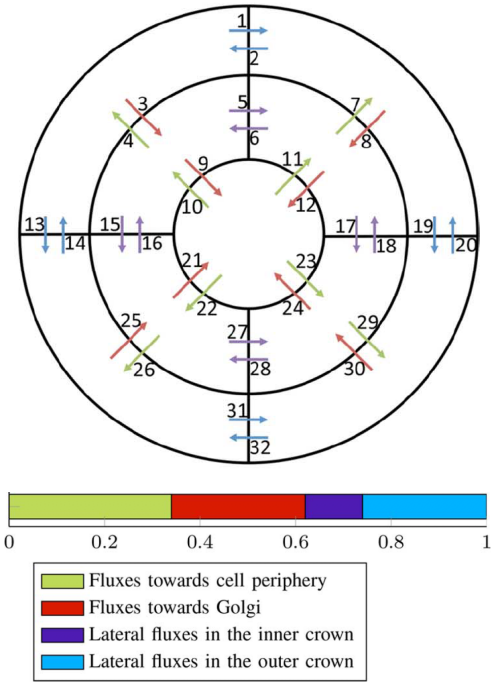

FIGURE 1.11 Cell partition of a disk-shaped cell and GFP-Rab6 vesicle flux estimation. (Top) The edge identification numbers are written next to each edge. Green edges are oriented towards the cell periphery, red edges are oriented towards the Golgi, purple edges correspond to lateral fluxes in the inner crown and blue edges to lateral fluxes in the outer crown. (Bottom) fluxes estimated over all registered sequences and grouped according to four different categories.

(MIP) and the Standard Deviation Intensity Projection (SDIP) maps defined as:

$$SDIP(I))(s) \quad = \quad \left(\frac{1}{T}\sum_{t=1}^{T}(I(s,t)-\bar{I}(s))\right)^{1/2} \tag{1.9}$$

where T denotes the number of images in the sequence, and $\bar{I}(s)$ represents the average intensity measured at pixel s. The MIP and SDIP maps computed from real and simulated image sequences are consistent as illustrated in Figs. 1.13 and 1.14 (bottom). The Golgi apparatus is characterized by a very bright spot on the projection maps, while vesicle trafficking is represented by a number of segments corresponding to fractions of vesicle trajectories.

Traffic estimation from simulated image sequences In the last experiment, we applied the NT-based analysis method [46] to simulate image sequences from the network and the image partition shown in Fig. 1.15. The simulated sequence consisting of about 300 2D frames, has been obtained as before. For

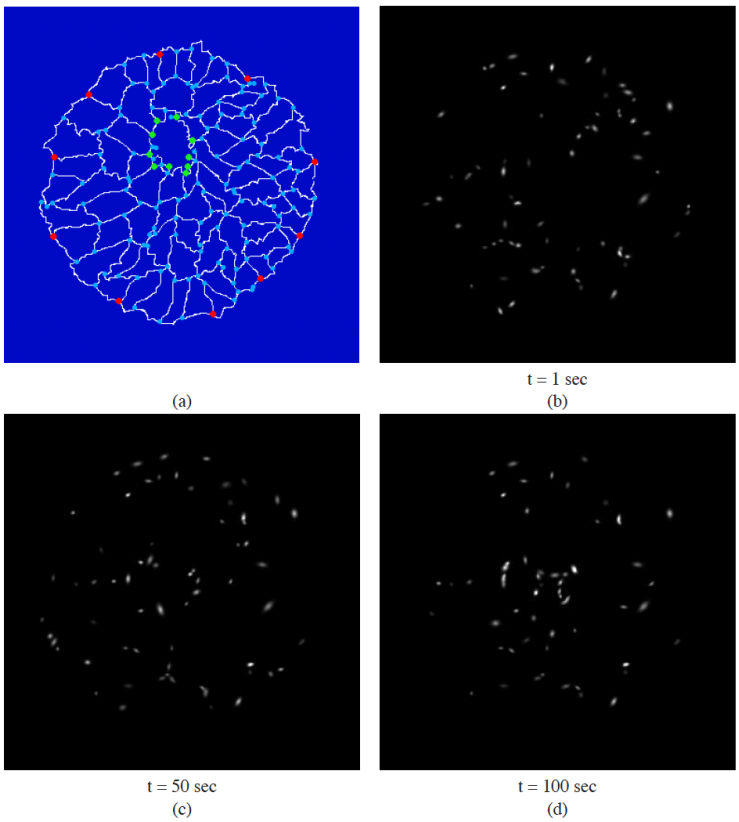

FIGURE 1.12 Simulation of GFP-Rab6 vesicles in a circular-shaped cell. (a) Microtubule network (white) and origin (green) and destination (red) nodes. (b)-(d) Three images extracted from the simulated sequence.

each generated vesicle, a destination among all the possible "end-points" is selected to ensure that the distribution of vesicles is uniform on all OD pairs. The segmentation of the OD regions has been achieved by manually partitioning the disk-shaped cell domain into 5 regions as illustrated with colors in Fig. 1.15 (right). In Fig. 1.16, we display the estimated OD flows (average proportions). In this experiment (5 image sequences), the algorithm [46] estimated the three OD pairs that were manually selected for simulation (ground truth). The algorithm which amounts to solving the optimization problem (1.3) presented in Section 1.1.3, was able to identify the main traffic directions.

RS = $64.5 \times 64.5nm^2$	Spatial resolution of the 2D simulated image
Δt = 1 sec	Time interval between two consecutive simulated images
$D_v \sim \mathcal{N}(180, 900)$	Size of Gaussian spots (vesicle)
$I_v \sim \mathcal{N}(25, 100)$	Intensity model of Gaussian spots
$V_v \sim \mathcal{N}(650, 2502)$	Velocity of vesicles
$P_{M \to S} = 0.7$	Probability for a vesicle to stop
$P_{s \to M} = 0.1$	Probability for a vesicle to re-start
$P_{PS} = 0.5$	Probability for vesicle to be in a "Pseudo-Stable" state
$P_{M \to PS} = 0.0004$	Probability for a vesicle to stop transiently
$P_F = 0.4$	Probability that a particle p_1 fuses with another particle p_2
$P_T = 0.001$	Probability that a vesicle moves back and takes another path
$T_P^{min}S$ = 30 sec	Lower bound of T_{PS}
T_{PS}^{max} = 100 sec	Upper bound of T_{PS}

TABLE 1.1 Default parameters used for GFP-Rab6 vesicle trafficking simulation.

1.4 CONCLUSION, FUTURE DIRECTIONS AND NEW CHALLENGES

We have described a general framework for traffic flow simulation in video-microscopy at the scale of a single cell. The method, based on the concept of Network Tomography mainly used in network communications, has been adapted to cell imaging and microscopy. It requires the extraction of origin-destination nodes automatically estimated or manually labelled by the user, as well as the setting of probabilities related "stop-and-go" events induced by traffic congestion. Background, noise and blur can be potentially added to produce more realistic images. We demonstrated the interest of the method for the modeling of GFP-Rab6 vesicle trafficking and the evaluation of image analysis algorithms. This approach is very flexible and can be adapted to many intracellular traffic simulations.

The limit of this simulation approach is related to the memory size needed to store the routing matrix and very large graphs with several thousands of nodes. In addition, additional efforts are required to extend the method dedicated to 2D+time image synthesis, to simulate temporal series of volumes for several minutes or hours as routinely acquired with microscopy set-ups. Finally, deep learning methods, including Generative Adversarial Networks [47], combined to Network tomography open new opportunities for data augmentation and data-driven simulation of biomolecule trafficking.

1.5 SUMMARY

The characterization of biomolecule dynamics is essential in cell biology since it offers a better understanding of fundamental mechanisms including membrane transport, cell signaling, cell division and motility. In that context, modeling and simulating trafficking of biomolecules has become helpful for prediction, data

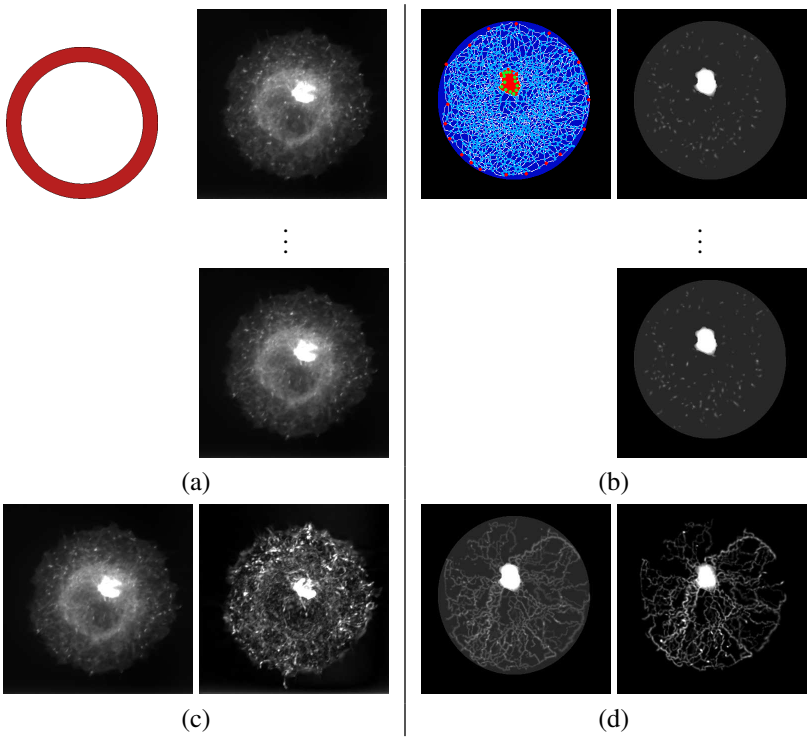

FIGURE 1.13 Comparison between real and simulated images depicting GFP-Rab6 vesicles in circular-shaped cells. (a) Circular micro-pattern (red) [40] and images extracted from a real image sequence. (b) Simulated images obtained from the network estimated by applying the algorithm [29] to the real image sequence shown in (a). The origin (green) and destination (red) nodes are superimposed on the microtubule network, at the center and the periphery of the cell, respectively. (c) MIP map and SDIP maps computed from 300 real images. (d) MIP and SDIP maps computed from 300 simulated images.

assimilation, learning, as well as for bioimage analysis algorithm evaluation. As the biomolecule transport in a cell can be interpreted as a vesicle trafficking depending on the organization of cytoskeleton components and regulated by specific proteins, we explored the potential of Network Tomography for image sequence simulation. As the network may be very complex, it is estimated from real microscopy images. The user then specifies the origin and destination nodes by labelling few nodes in the graph, and adds event features, depending on prior knowledge in cell biology. The resulting simulation algorithm is data-driven and is able to generate artificial 2D image sequences depicting fluorescently tagged proteins in video-microscopy.

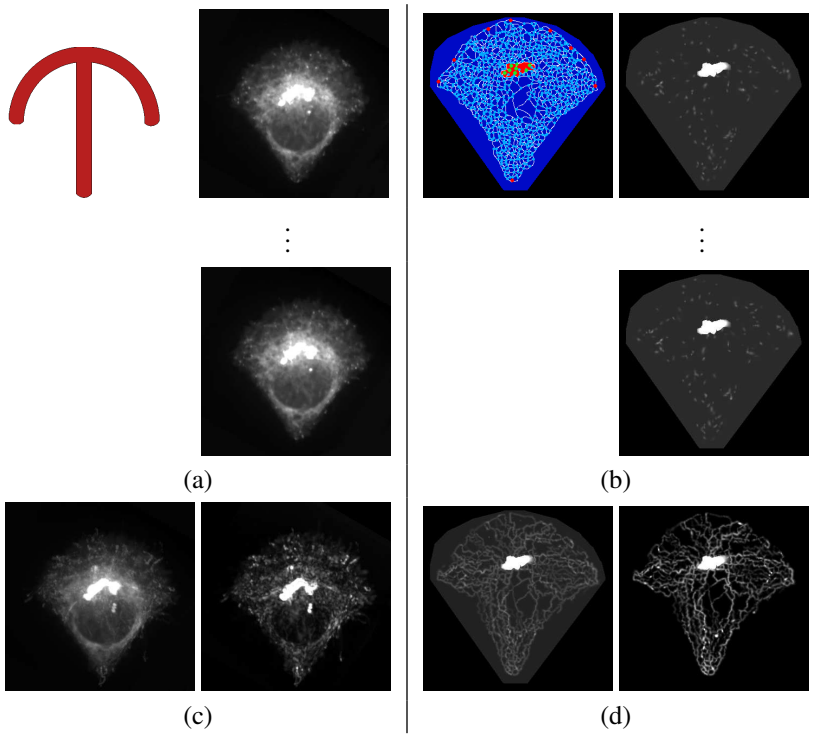

FIGURE 1.14 Comparison between real and simulated images depicting GFP-Rab6 vesicles in crossbow-shaped cells. (a) Crossbow micro-pattern (red) [40] and images extracted from a real image sequence. (b) Simulated images obtained from the network estimated by applying the algorithm [29] to the real image sequence shown in (a). The origin (green) and destination (red) nodes are superimposed on the microtubule network, at the center and the periphery of the cell, respectively. (c) MIP map and SDIP maps computed from the real image sequence (a). (d) MIP and SDIP maps computed from 300 simulated images.

ACKNOWLEDGMENT

The author thanks very warmly Jean Salamero, Thierry Pécot, and Jérôme Boulanger, as well as the members of the Serpico and STED teams, and of the PiCT IBiSA facility, who participated to this project started a few years ago.

This work was supported by Inria Rennes computing grid facilities partly funded by France-BioImaging infrastructure (French National Research Agency - ANR-10-INBS-04-07, “Investments for the future”).

REFERENCES

[1] P. Bressloff, J. Newby, Stochastic models of intracellular transport, Rev. Mod. Phys. 85 (135) (2013) 135–196.

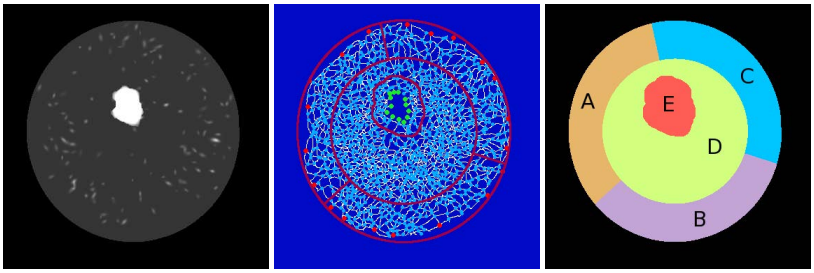

(a) (b) (c)

OD pair number	OD pair	OD pair number	OD pair
0	$A \to B$	10	$C \to E$
1	$A \to C$	11	$C \to D$
2	$A \to D$	12	$D \to A$
3	$A \to E$	13	$D \to B$
4	$B \to A$	14	$D \to C$
5	$B \to C$	15	$D \to E$
6	$B \to D$	16	$E \to A$
7	$B \to E$	17	$E \to B$
8	$C \to A$	18	$E \to C$
9	$C \to B$	19	$E \to D$

FIGURE 1.15 Simulated image sequences for NT estimation. (Top) Simulated image (a) extracted from a sequence obtained from the network shown in (b). The nodes and edges are labelled in blue and white, respectively. The origin (green) and destination (red) are located at the center and at the periphery of the circular-shaped cell, respectively. (c) Manual partition of the cell domain into 5 regions. The central region is compelled to be an origin region. (Bottom) List of 20 possible OD pairs.

[2] N. Hozé, D. Holcman, Statistical methods for large ensembles of super-resolution stochastic single particle trajectories in cell biology, Annual Reviews 4 (2017) 189–223.

[3] V. Briane, C. Kervrann, M. Vimond, Statistical analysis of particle trajectories in living cells, Physical Review E 97 (6-1) (2018) 062121.

[4] V. Briane, M. Vimond, C. Kervrann, An overview of diffusion models for intracellular dynamics analysis, Briefings in Bioinformatics 21 (4) (2020) 1136–1150.

[5] N. Chenouard, I. Smal, F. de Chaumont, M. Maška, I. Sbalzarini, Y. Gong, J. Cardinale, C. Carthel, S. Coraluppi, M. Winter, A. Cohen, W. Godinez, K. Rohr, Y. Kalaidzidis, L. Liang, , J. Duncan, H. Shen, Y. Xu, K. Magnusson, J. Jaldén, H. Blau, P. Paul-Gilloteaux, P. Roudot, C. Kervrann, F. Waharte, J. Tinevez, S. Shorte, J. Willemse, K. Celler, G. van Wezel,

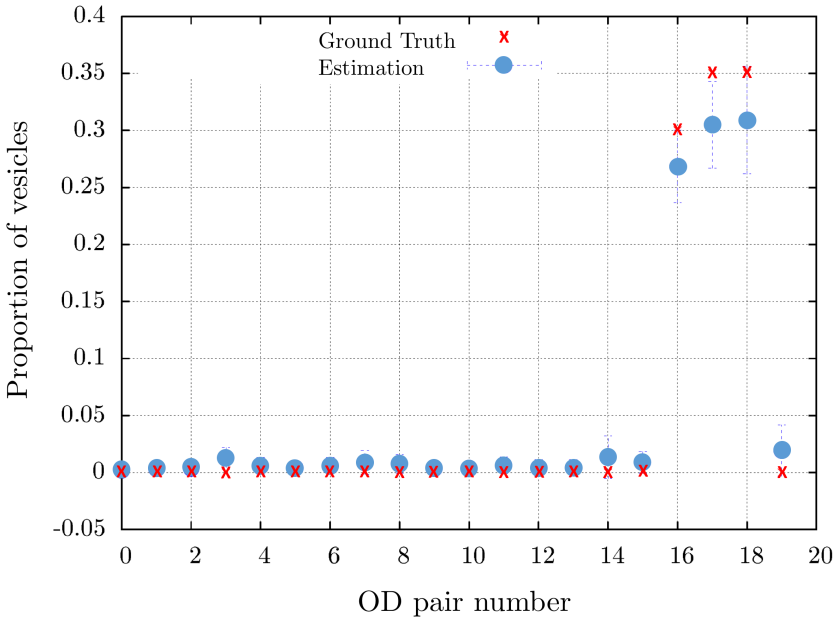

FIGURE 1.16 OD pair estimation on simulated sequences. Averaged proportions of OD pairs (with variance) from five simulated image sequences (see Fig. 1.15).

H. Dan, Y. Tsai, C. Ortiz de Solórzano, J.-C. Olivo-Marin, E. Meijering, Objective comparison of particle tracking methods, Nat. Methods 11 (3) (2014) 281–289.

[6] C. Anderson, G. Georgiou, I. Morrison, G. Stevenson, R. Cherry, Tracking of cell surface receptors by fluorescence digital imaging microscopy using a charged-coupled device camera. low-density lipoprotein and influenza virus receptor mobility at 4 degrees c, J. Cell Science 101 (1992) 415–425.

[7] I. Sbalzarini, P. Koumoutsakos, Feature point tracking and trajectory analysis for video imaging in cell biology, J. Struct. Biol. 151 (2) (2005) 182–195.

[8] V. Racine, A. Hertzog, J. Jouaneau, J. Salamero, C. Kervrann, J. Sibarita, Mutliple target tracking of 3d fluorescent objects based on simulated annealing, in: Proc. Int. Symp. Biomedical Imaging (ISBI), Washington, USA, 2006, pp. 1020–1023.

[9] I. Smal, M. Loog, W. Niessen, E. Meijering, Quantitative comparison of spot detection methods in fluorescence microscopy, IEEE Trans. Med. Imaging 29 (2) (2010) 282–301.

[10] C. Kervrann, C. Sorzano, S. Acton, J.-C. Olivo-Marin, M. Unser, A guided tour of selected image processing and analysis methods for fluorescence and electron microscopy, IEEE J. Selected Topics Signal Process. 10 (1) (2016) 6–30.

[11] N. Chenouard, I. Bloch, J.-C. Olivo-Marin, Multiple hypothesis tracking for cluttered biological image sequences, IEEE Trans. Patt. Anal. Mach. Intell. 35 (11) (2013) 2736–2750.

[12] L. Liang, H. Shen, P. De Camilli, J. Duncan, A novel multiple hypothesis based particle tracking method for clathrin mediated endocytosis analysis using fluorescence microscopy, IEEE Trans. Image Process. 23 (4) (2014) 1844—-1857.

[13] I. Smal, E. Meijering, K. Draegestein, N. Galjart, I. Grigoriev, A. Akhmanova, M. van Royen, A. Houtsmuller, W. Niessen, Multiple object tracking in molecular bioimaging by rao-blackwellized marginal particle filtering, Med. Image Analysis 12 (6) (2008) 764–777.

[14] K. Jaqaman, D. Loerke, M. Mettlen, H. Kuwata, S. Grinstein, S. Schmid, G. Danuser, Robust single-particle tracking in live-cell time-lapse sequences, Nat. Methods 5 (2008) 695–702.

[15] P. Roudot, L. Ding, K. Jaqaman, C. Kervrann, G. Danuser, Piecewise-stationary motion modeling and iterative smoothing to track heterogeneous motion in dense intracellular environments, IEEE Trans. Image Process. 26 (11) (2017) 5395–5410.

[16] R. Spilger, A. Imle, J. Lee, B. Muller, O. Fackler, R. Bartenschlager, Rohr, A recurrent neural network for particle tracking in microscopy images using future information, track hypotheses, and multiple detection, IEEE Trans. Image Process. 29 (2020) 3681—-3694.

[17] E. Cascetta, S. Nguyen, A unified framework for estimating or updating origin/destination matrices from traffic counts, Transportation Research 22 (6) (1988) 437–455.

[18] H. Spiess, A maximum likelihood model for estimating origin-destination matrices, Transportation Research 21 (5) (1987) 395–412.

[19] Y. Vardi, Network tomography: Estimation source-destination traffic intensities from link data, J. American Statistical Association 91 (433) (1996) 365–377.

[20] E. Dijkstra, A note on two problems in connexion with graphs, Numerische Mathematik 1 (1) (1959) 269–271.

[21] M. Lagardère, I. Chamma, E. Bouilhol, M. Nikolski, O. Thoumine, Fluosim: simulator of single molecule dynamics for fluorescence live-cell and super-resolution imaging of membrane proteins, Scientific Reports 10 (19954) (2020) 1–14.

[22] A. Badoual, M. Arizono, A. Denizot, M. Ducros, H. Berry, V. Nägerl, C. Kervrann, Simulation of astrocytic calcium dynamics in lattice light sheet microscopy images, in: Proc. Int. Symp. Biomedical Imaging (ISBI), Nice, France, 2021.

[23] A. Genovesio, T. Liedl, V. Emiliani, W. Parak, M. Coppey-Moisan, J.-C. Olivo-Marin, Multiple particle tracking in 3D+t microscopy: method and application to the tracking of endocytosed quantum dots, IEEE Trans. Image Process. 15 (5) (2006) 1062–1070.

[24] T. Lagache, E. Dauty, D. Holcman, Quantitative analysis of virus and plasmid trafficking in cells, Physical Review E 79 (1) (2009) 011921.

[25] M. Klann, H. Koeppl, M. Reuss, Spatial modeling of vesicle transport and the cytoskeleton: the challenge of hitting the right road, PLoS One 7 (1) (2012) e29645.

[26] F. Gibbons, J. Chauwin, M. Despósito, J. José, A dynamical model of kinesin-microtubule motility assays, Biophysical J. 80 (6) (2001) 2515—-2526.

[27] F. Nédélec, Computer simulations reveal motor properties generating stable antiparallel microtubule interactions, J. Cell Biol. 158 (6) (2001) 1005–1015.

[28] P. Allain, C. Kervrann, Physical modeling of microtubules network, in: Proc. Int. Workshop New Computational Methods for Inverse Problems (NMCIP), Paris, France, 2014.

[29] C. Steger, An unbiased detector of curvilinear structures, IEEE Trans. Patt. Anal. Mach. Intell. 20 (2) (1998) 113–125.

[30] C. Bergsma, G. Streekstra, A. Smeulders, E. Manders, Velocity estimation of spots in 3d confocal image sequences of living cells, Cytometry 53 (4) (2001) 261–272.

[31] T. Pécot, P. Bouthemy, J. Boulanger, A. Chessel, S. Bardin, J. Salamero, C. Kervrann, Background fluorescence estimation and vesicle segmentation in live cell imaging with conditional random fields, IEEE Trans. Image Process. 24 (2) (2015) 667–680.

[32] J. Yen, Finding the k shortest loopless paths in a network', Management Science 17 (1971) 712–716.

[33] A. Brown, L. Wang, P. Jung, Stochastic simulation of neurofilament transport in axons : The "stop-and-go" hypothesis, Mol. Biol. of the Cell 16 (9) (2005) 4243—-4255.

[34] J. White, L. Johannes, F. Mallar, A. Girod, G. Stephan, S. Reinsh, P. Keller, B. Tzschaschel, A. Echard, B. Goud, E. Stelzer, Rab6 coordinates a novel golgi to ER retrograde transport pathway in live cells, The Journal Cell Biol. 147 (4) (1999) 743–760.

[35] P. Chavrier, B. Goud, The role of arf and rab gtpases in membrane transport, Current Opinion in Cell 11 (4) (1999) 466–475.

[36] F. Opdam, A. Echard, J. Croes, H.J. and. van den Hurk, R. van de Vorstenbosch, L. Ginsel, B. Goud, J. Fransen, The small gtpase rab6b, a novel rab6 subfamily member, is cell-type specifically expressed and localised to the golgi apparatus, J. Cell Sci. 113 (15) (2000) 2725—2735.

[37] A. Echard, F. Opdam, H. de Leeuw, F. Jollivet, P. Savelkoul, W. Hendriks, J. Voorberg, B. Goud, J. Fransen, Alternative splicing of the human rab6a gene generates two close but functionally different isoforms, Mol. Biol. of the cell 11 (2000) 3819–3833.

[38] I. Grigoriev, D. Splinter, N. Keijzer, P. Wulf, J. Demmers, T. Ohtsuka, M. Modesti, I. Maly, F. Grosveld, C. Hoogenraad, A. Akhmanova, Rab6 regulates transport and targeting of exocytotic carriers, Developmental Cell 13 (2) (2007) 305–314.

[39] S. Bardin, S. Miserey-Lenkei, I. Hurbain, D. Garcia-Castillo, G. Raposo, G. B., Phenotypic characterisation of rab6a knockout mouse embryonic fibroblasts, Biology of the Cell 107 (12) (2015) 427—-439.

[40] M. Théry, V. Racine, A. Pépin, M. Piel, Y. Chen, J.-B. Sibarita, M. Bornens, The extracellular matrix guides the orientation of the cell division axis, Nat. Cell Biology 7 (10) (2005) 947–953.

[41] K. Schauer, T. Duong, K. Bleakley, S. Bardin, M. Bornens, B. Goud, Probabilistic density maps to study global endomembrane organization, Nat. Methods 7 (7) (2010) 560—-566.

[42] K. Schauer, T. Duong, C. Gomes-Santos, B. Goud, Studying intracellular trafficking pathways with probabilistic density maps,, Methods Cell Biol. 118 (2013) 325–343.

[43] T. Pécot, L. Zengzhen, J. Boulanger, F. Waharte, J. Salamero, C. Kervrann, A quantitative approach for analyzing the spatio-temporal distribution of 3d intracellular events in fluorescence microscopy, ELife 7 (2018) e32311.

[44] A. Basset, J. Boulanger, J. Salamero, P. Bouthemy, C. Kervrann, Adaptive spot detection with optimal scale selection in fluorescence microscopy images, IEEE Trans Image Process. 24 (11) (2015) 4512–4527.

[45] T. Pécot, C. Kervrann, J. Salamero, J. Boulanger, Counting-based particle flux estimation for traffic analysis in live cell imaging, IEEE J. Selected Topics in Signal Process. 10 (1) (2016) 203–216.

[46] T. Pécot, C. Kervrann, P. Bouthemy, Minimal paths and probabilistic models for origin-destination traffic estimation in live cell imaging, in: Proc. Int. Symp. Biomedical Imaging (ISBI), Paris, France, 2008, pp. 843–846.

[47] I. Goodfellow, J. Pouget-Abadie, M. Mirza, B. Xu, D. Warde-Farley, S. Ozair, A. Courville, Y. Bengio, Generative adversarial networks, in: Proc. of Int. Conf. Neural Information Processing Systems (NIPS), Montreal, Canada, 2014, p. 2672–2680.

FURTHER READING

- Serpico Website: https://team.inria.fr/serpico/publications/
- J. Boulanger. **Estimation non-paramétrique et contributions à l'analyse de séquences d'images. Modélisation, simulation et estimation du trafic intra-cellulaire dans des séquences de vidéo-microscopie.** Thèse de l'université de Rennes 1, Mention Traitement du Signal et des Télécommunications, 2007. (in French)
- T. Pécot. **Modélisation et estimation du trafic intracellulaire par tomographie de réseaux et microscopie de fluorescence.** Thèse de l'université de Rennes 1, Mention Traitement du Signal et des Télécommunications, 2010. (in French)